Auxiliary Material for "The 2010 Maule, Chile earthquake: Downdip rupture limit revealed by space geodesy"

Xiaopeng Tong[1], David Sandwell[1], Karen Luttrell[1], Benjamin Brooks[2], Michael Bevis[3], Masanobu Shimada[4], James Foster[2], Robert Smalley Jr.[5], Hector Parra[6], Juan Carlos Báez Soto[7], Mauro Blanco[8], Eric Kendrick[3], Jeff Genrich[9], Dana J. Caccamise II[3]

[1]Scripps Institution of Oceanography, University of California San Diego, La Jolla, CA 92093-0225 USA

[2]Hawaii Institutes of Geophysics and Planetology, University of Hawaii, Honolulu, HI 96822 USA

[3]School of Earth Science, Ohio State University, 125 South Oval 275 Mendenhall Laboratory, Columbus, OH 43210, USA

[4]Japan Aerospace Exploration Agency, Earth Observation Research Center, Tsukuba Ibaraki, 350-8505, Japan

[5]Center for Earthquake Research and Information, University of Memphis, 3876 Central Ave Ste 1, Memphis, TN, 38152-3050, USA

[6]Instituto Geográfico Militar Chile, Dieciocho No 369, Santiago, Chile.

[7]Universidad de Concepción, Campus Los Angeles, J. A. Coloma 0201, Los Angeles, Chile

[8]Instituto CEDIAC, Facultad de Ingeniería, Universidad Nacional de Cuyo, CC405 CP5500, Mendoza, Argentina

[9]Division of Geological and Planetary Science, California Institute of Technology, Pasadena, CA 91125 US

This supplementary material provides details on the GPS and InSAR data analysis, including the temporal and spatial coverage of the InSAR and GPS data, data misfit and inversion method (see Table S1 and Table S2). The radar line-of-sight displacement measurements and their residuals are summarized in Figure S1 and S2. Our conclusions regarding the variations in slip with depth and the estimate of near-zero slip below ~45 km depth depend on the coverage and accuracy of the geodetic data as well as the characteristics of the model. We investigated the effects of the smoothness parameter on the spatial resolution of the model (see Figure S3). In addition, the supplementary material describes our inversion method and synthetic resolution tests in greater detail to assist the evaluation of the slip model (see Figure S4, S5, S6).

GPS Data Analysis

All available continuous GPS data in South America from 2007 through 2010 May 5 were processed using GAMIT [*King and Bock*, 2000] with additional GPS sites included to provide reference frame stability (Table S1). All data were processed using the MIT precise orbits. Orbits were held tightly constrained and standard earth orientation parameters (EOP) and earth and ocean tides were applied. Due to the number of stations, two separate subnets were formed with common fiducial sites. The subnets were merged and combined with MIT's global solution using GLOBK. We defined a South American fixed reference frame, primarily from the Brazilian craton, to better than 2.4 mm/yr RMS horizontal velocity by performing daily Helmert transformations for the network solutions and stacking in an ITRF2005 reference frame [*Kendrick, et al.*, 2006]. Finally we used these time series to estimate the coseismic displacement, or jumps, at each station affected by the Maule event, as well as crustal velocity before and after the earthquake.

InSAR Phase Unwrapping and Adjustment

We unwrapped all the interferograms by digitizing and counting fringes at every 2π phase cycle (11.8 cm) (see Figure S1) [*Tong et al.,* 2010]. This method works well even in low coherence areas, such as ScanSAR-ScanSAR interferograms (see Figure 1, T422-sw3). We assembled all the digitized fringes, subsampled them using a blockmedian average with pixel spacing of 0.05° in latitude and 0.1° in longitude, and converted them into line of sight (LOS) displacement. The interferograms are subject to propagation delay through the atmosphere and ionosphere. It is likely that T112 and parts of T116 include significant (> 10 cm) ionospheric delay, so these data were excluded from the analysis (see Figure S1a and Table S2). To account for the potential errors in digitization and propagation delay effects, we assigned a uniform uncertainty of 10 cm to the LOS data. Interferometry is a relative measurement of LOS displacement, so after unwrapping the average value of each track was adjusted to match the available GPS displacement vectors projected into the LOS direction. For tracks that do not contain a GPS station, their average value was adjusted so that the LOS displacement field is mostly continuous from track to track. Over a distance of up to 1000 km the satellite orbits are much more accurate than the 10 cm assigned uncertainty [*Sandwell et al.,* 2008] so no linear ramp was removed from the unwrapped and sampled LOS displacement data. Even after adjustment, the phase between neighboring tracks is sometimes discontinuous, as seen, for example, at the southern end of the descending interferograms (see Figure 1b and Figure S1b) where the fringes are denser in T422-sw4 than T420. This is partially due to the difference in look angle between the far range in one track and the near range of the adjacent track. This kind of discontinuity can also be caused by rapid and significant postseismic deformation between the acquisition times of the adjacent SAR tracks. The final step in the processing was to calculate the unit look vector between each LOS data point and the satellite using the precise orbits. This is needed to project the vector deformation from a model into the LOS direction of the measurement.

Uncertainty in GPS and InSAR data

When calculating the weighted residual misfit, we estimated the uncertainty of the geodetic measurement. Errors in the GPS measurement were calculated using residual scatter values (Table S1). Errors in the InSAR LOS displacement measurement were assigned uniformly as 10 cm based on posteriori misfit.

Model optimization

The model consists of a 670 km long and 260 km wide 15° dipping fault plane in a homogeneous elastic half-space (Figure S3). The fault plane is subdivided into 19.7 km by 20 km patches. The fault patch size was chosen to retrieve major features in the slip model while keeping the inversion problem manageable. We applied a non-negativity constraint to allow only thrust and right-lateral strike slip; only the bottom boundary of the fault plane is constrained to have zero slip. The minimization criteria is given by the equation

$$\min(\|Am - b\|^2 + \lambda^2 \|Sm\|^2) \quad (1)$$

where the first term minimizes the data misfit and the second term minimizes model roughness (i.e., second derivative) of slip on the fault plane. In the first term, A is the inversion matrix, m is the vector of unknowns, and b is the matrix of observations, given by

$$A = \begin{bmatrix} \sigma_{LOS}{}^{-1} G_{LOS} \\ \beta \sigma_{GPS}{}^{-1} G_{GPS} \end{bmatrix},\ m = \begin{bmatrix} m_{dip} \\ m_{strike} \end{bmatrix},\ b = \begin{bmatrix} \sigma_{LOS}{}^{-1} d_{LOS} \\ \beta \sigma_{GPS}{}^{-1} d_{GPS} \end{bmatrix} \quad (2)$$

The A matrix consists of the Green's function matrices G_{LOS} and G_{GPS} weighted by the uncertainties in the measurements. The two diagonal matrices σ_{LOS} and σ_{GPS} are derived from measurement uncertainties, and β represents the relative weight between InSAR and GPS data sets. The model vectors m_{dip} and m_{strike} represent dip-slip components and strike-slip components on discretized fault patches. In matrix b, the observation vectors d_{LOS} and d_{GPS} consist of the InSAR data, which are the LOS displacement from the ascending and descending tracks, and the GPS data with east-north-up displacement components. In the second term the smoothness matrix is given by

$$S = \begin{pmatrix} -1 & 4 & -1 & 0 & \ldots \\ 0 & -1 & 4 & -1 & \ldots \\ 0 & 0 & -1 & 4 & -1 \\ \ldots & \ldots & \ldots & \ldots & \ldots \end{pmatrix}. \qquad (3)$$

The relative weighting between GPS and InSAR data, parameter β, is determined iteratively so that the residuals are minimized in both datasets. We select the relative weighting between the data misfit and roughness, parameter λ, based on the trade-off curve between model smoothness and the normalized RMS misfit. Nine different weights were tested and the preferred model is chosen at the turning point of this trade-off curve (Figure S3). While the selection of the best model is somewhat subjective, all the models share a common characteristic of high depth-averaged slip at an along-dip distance of 60-100 km and essentially zero slip at ~160 km.

Resolution tests

To assess the resolution capabilities of the data and model, we conducted two sets of checkerboard tests. The first test had a 20 km checkerboard of 500 cm in dip slip (Figure S4). The checkerboard model was used to generate synthetic InSAR and GPS data at the observation locations. The InSAR, and GPS data were assigned the same uncertainties as used in the final model. We inverted for a best fitting solution by adjusting the smoothness parameter while retaining all the other parameter settings as were used in the final model (Figure S4).

We found that the resolution is better over the southern half of the fault plane where there is more complete InSAR coverage closer to the trench axis. We calculated the RMS of the slip difference (i.e. a measure of the misfit) between the synthetic model and the recovered model, averaged over the fault strike direction. Plots of RMS slip difference versus depth (Figure S6) show a minimum at a downdip distance of 120 km. The accuracy of the recovered model is good between downdip distances of 110 and 130 km where the average RMS curve falls below 100 cm. Over this depth range features as small as 20 km can be resolved to a 20% accuracy.

We repeated the checkerboard test at a size of 40 km as shown in Figure S5. The accuracy of the recovered checkerboard improves significantly when the checker size is increased from 20 km to 40 km. We calculated the RMS of the slip difference in the same way as for the 20 km checker size (see Figure S6). The accuracy of the recovered model is good between downdip distances of 70 and 220 km where the average RMS curve falls below 100 cm, corresponding to the area where the recovered model uncertainties are less than 20% of the input model. The accuracy is excellent between the downdip distances of 80 and 190 km where the average RMS curve falls below 50 cm, corresponding to the area where the recovered model uncertainties are less than 10% of the input model. From these checkerboard tests we conclude that the overall model resolution is 40 km or better over the downdip width range of 70 to 220 km.

Determination of shear modulus

Our model requires a representative value of shear modulus in order to calculate the geodetic moments from the slip model, although the Okada's displacement solution only depends on the Poisson's ratio. We determined the average shear modulus from regional 1D seismic velocity structure [*Bohm et al*., 2002]. Above 45 km depth, the average shear modulus (weighted by layer thickness) is 38.3 GPa. Above 55km depth, the average shear modulus (weighted by layer thickness) is 43.5 GPa. Thus an average shear modulus of 40 GPa is a preferred value for estimating geodetic moment (Table S3).

Supplementary References

Bohm, M., et al., (2002), The Southern Andes between 36° and 40° latitude: seismicity and average seismic velocities. Tectonophys, 356(4):275–289

Kendrick, E., et al. (2006), Active Orogeny of the South-Central Andes Studied With GPS Geodesy, Revista de la Asociación Geológica Argentina, 61 (4), 555-566

King, R., and Y. Bock (2000), Documentation for the GAMIT GPS Analysis Software, Massachusetts Institute of Technology and Scripps Institute of Oceanography, Cambridge, Mass.

Sandwell, D.T., et al. (2008), Accuracy and Resolution of ALOS Interferometry: Vector Deformation Maps of the Father's Day Intrusion at Kilauea, IEEE Trans. Geosci. Remote Sens., 46(11), 3524-3534.

Tong, X., D. T. Sandwell and Y. Fialko (2010), Coseismic slip model of the 2008 Wenchuan earthquake derived from joint inversion of interferometric synthetic aperture radar, GPS, and field data, J. Geophys. Res., 115, B04314, doi:10.1029/2009JB006625.

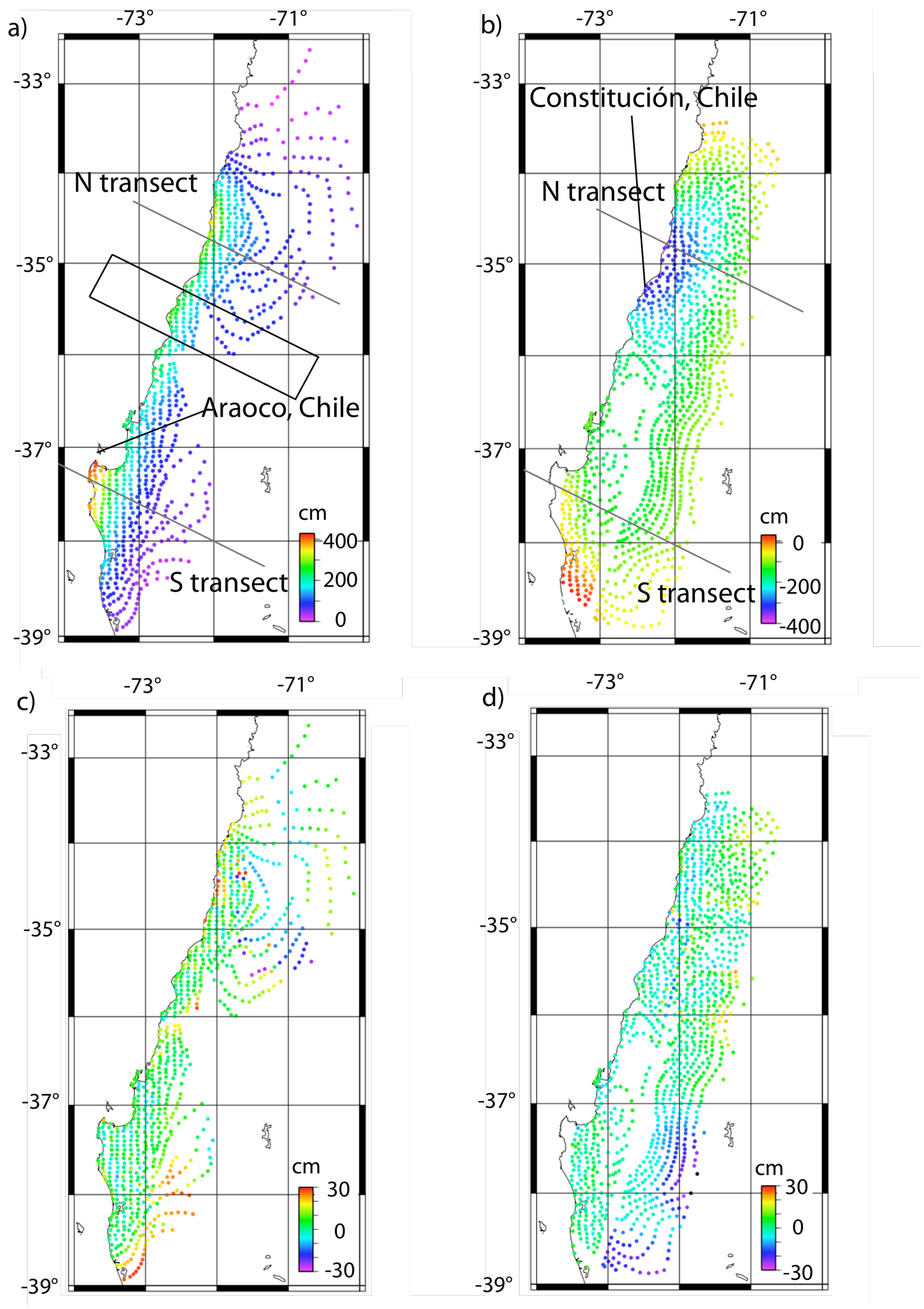

Figure S1. Unwrapped, subsampled, and calibrated InSAR line-of-sight (LOS) displacements and their residuals. Positive LOS displacement indicates ground motion toward the radar. a) Ascending LOS displacement. b) Descending LOS displacement. c) Model residuals of the ascending LOS displacement. d) Model residual of the descending LOS displacement. The two black lines (N transect and S transect) mark the locations of profiles shown in Figure 2a and Figure 2b. The black box in subplot a) shows the sampled area of topography and gravity profiles as shown in Figure S2c.

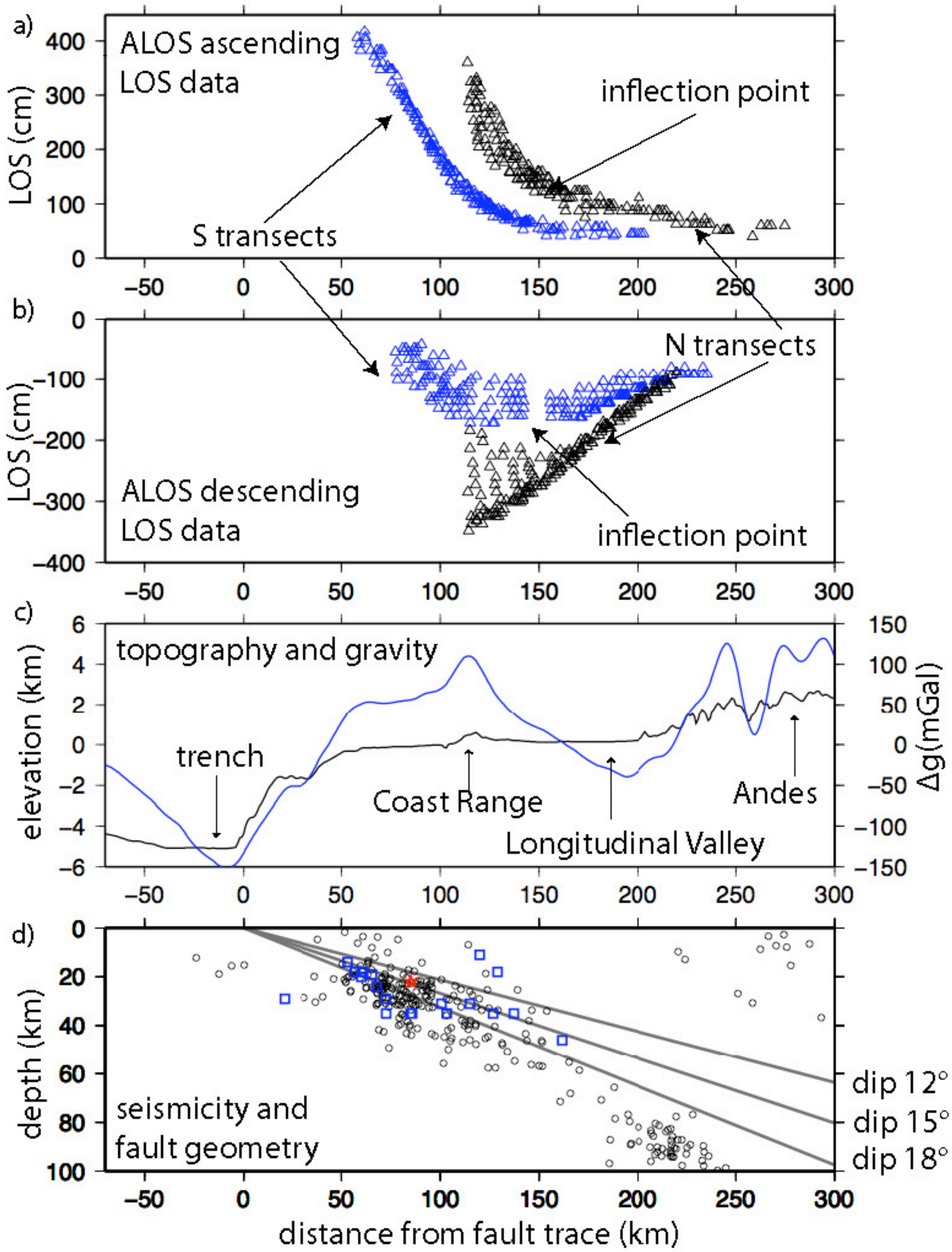

Figure S2. Transects of unwrapped line-of-sight data a) ascending and b) descending. Locations of north (black) and south (blue) transects are shown in Figure S1. c) Topography (black line) and free-air gravity (blue line) profiles over Chile illustrate the major geological features. d) Seismicity and fault geometry. The black circles show the background seismicity, the red star shows the epicenter, and the blue squares show the locations of the M>6 aftershocks from the PDE catalog [*NEIC*, 2010].

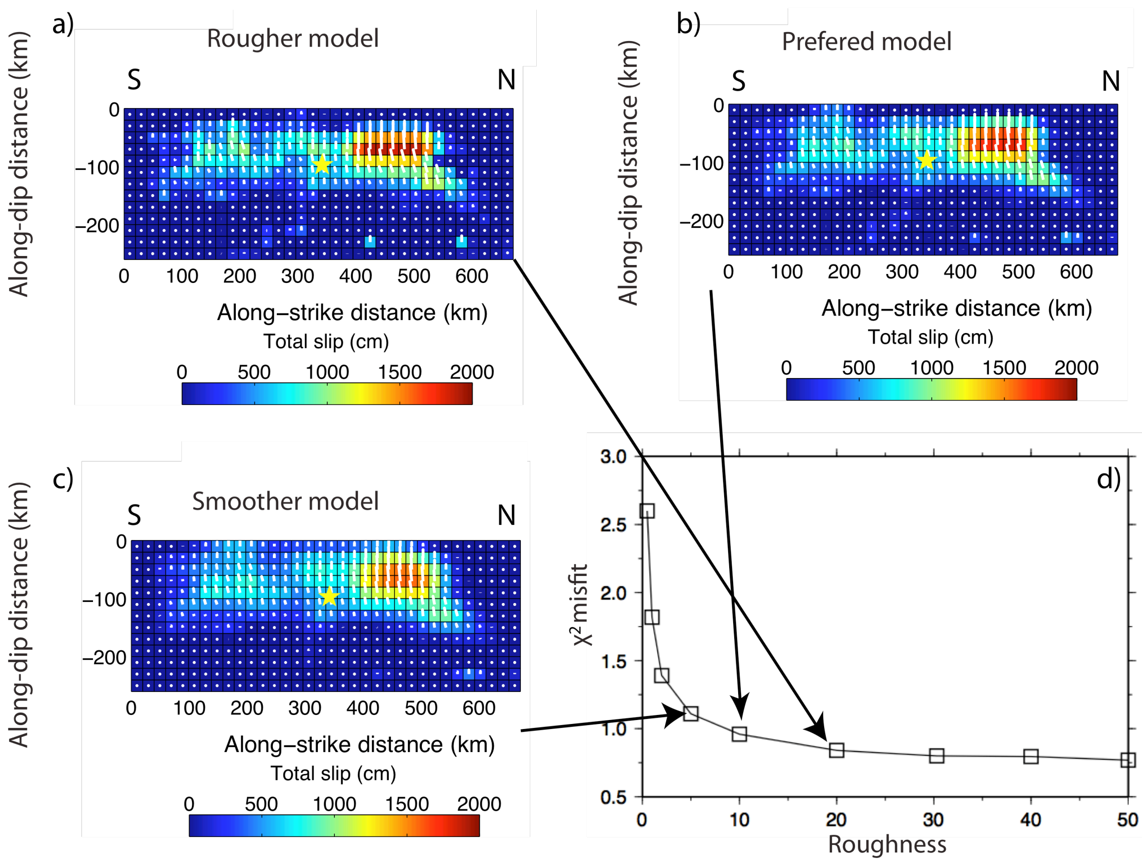

Figure S3. Slip models with three different weights on the smoothing function. The total slip magnitude on fault patches are represented by the color. In each slip model, the white lines, which originate from center of the rectangular patches and point outward, illustrate the relative motion of the hanging wall with respect to the footwall (mainly thrust slip with small right-lateral strike slip in this case). The yellow star is the position of the main shock. a) A rougher model. b) Our preferred model. c) A smoother model. d) The trade-off curve showing the χ^2 misfit versus the roughness.

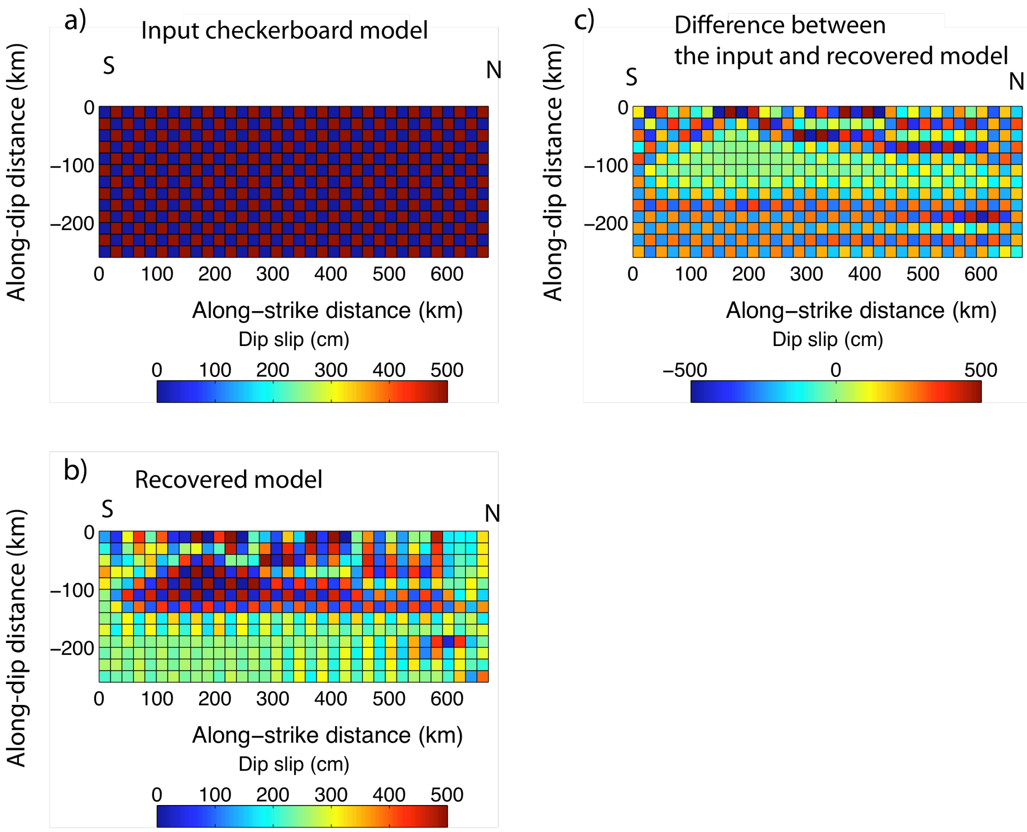

Figure S4. Resolution test with checker size of 20 km. a) Synthetic input model has thrust displacement of either zero or 500 cm spaced at 20 km intervals . b) The recovered model. c) The difference between the synthetic input model and the recovered model.

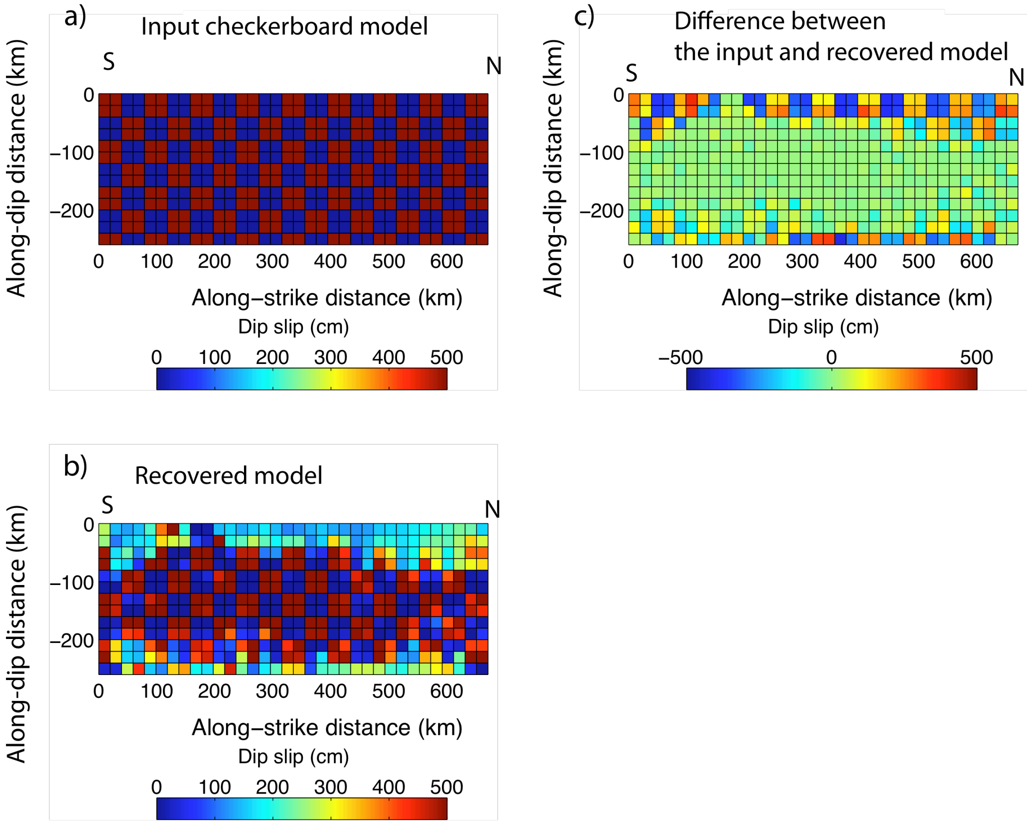

Figure S5. Resolution tests with checker size of 40 km. a) Synthetic input model that has thrust displacement of either zero or 500 cm spaced at 40 km intervals. b) The recovered model. c) The difference between the synthetic input model and the recovered model.

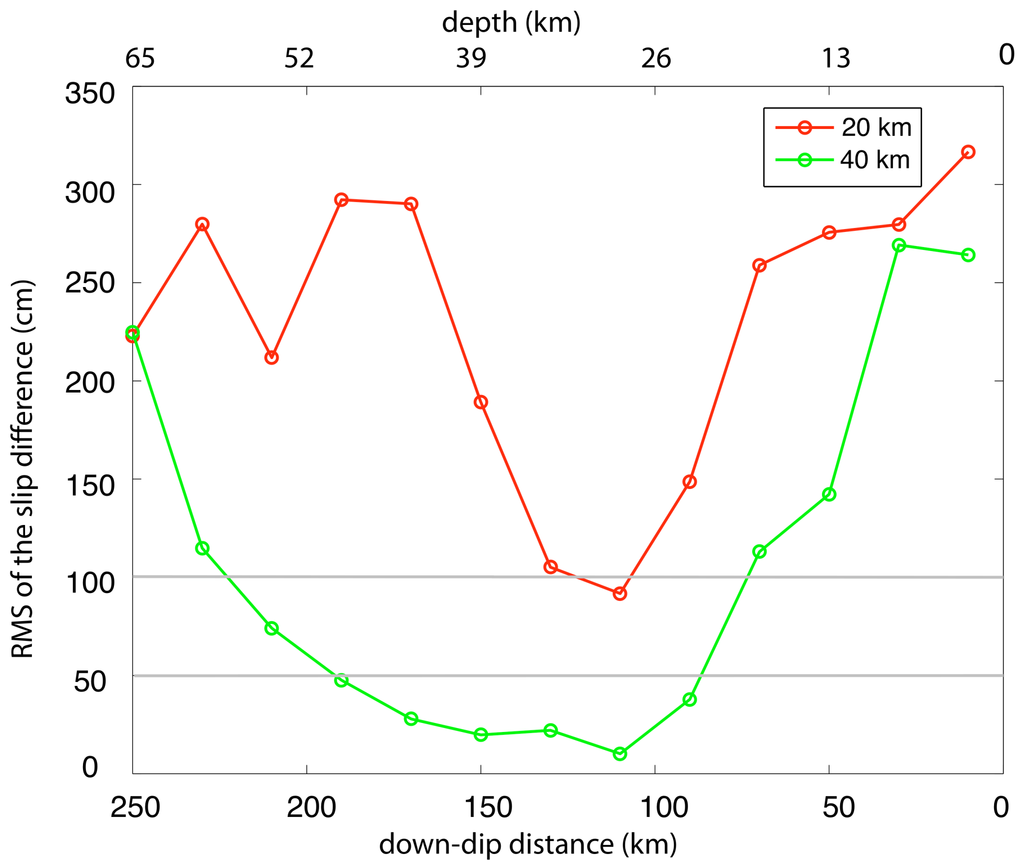

Figure S6. Accuracy of slip recovery versus downdip distance for 20 km (red line) and 40 km (green line) checker sizes. The RMS slip difference is the along-strike average of slip differences shown in Figure S4 (red line) and Figure S5 (green line). The horizontal axis shows the downdip distance (below) and depth (above). We set 20% RMS of the slip difference as the accuracy threshold so in this case the model is resolved at 20 km between downdip distances of 110 and 130 km and the model is resolved at 40 km between downdip distances of 70 and 220 km.

Table S1. GPS measurements used in this study and their fits to the model.

			east displacement (cm)		north displacement (cm)		up displacement (cm)	
name	longitude	latitude	data	model	data	model	data	model
ANTC	-71.532	-37.338	-80.62 ± 0.41	-81.62	18.37 ± 0.35	17.90	-2.73 ± 1.22	-5.48
CONZ	-73.025	-36.843	-300.19 ± 1.49	-300.15	-67.76 ± 1.33	-67.89	-3.98 ± 2.04	-4.28
MZ04	-69.020	-32.948	-12.17 ± 0.51	-15.20	-4.93 ± 0.32	-5.68	1.89 ± 1.13	-1.20
SANT	-70.668	-33.150	-23.53 ± 1.46	-25.19	-14.07 ± 1.12	-14.24	-1.76 ± 1.88	-5.88
LNQM	-71.361	-38.455	-33.44 ± 0.57	-34.67	14.31 ± 0.42	14.32	0.47 ± 1.34	-3.85
MZ05	-69.169	-32.951	-12.63 ± 0.53	-15.77	-5.19 ± 0.32	-6.15	1.79 ± 1.04	-1.46
ACPM	-70.537	-33.447	-41.49 ± 0.51	-40.24	-18.55 ± 0.33	-18.20	-1.90 ± 1.07	-5.96
BAVE	-70.765	-34.167	-116.61 ± 0.17	-116.57	-19.49 ± 0.17	-19.49	-9.44 ± 0.67	-9.94
LAJA	-71.376	-37.385	-72.18 ± 0.45	-71.77	17.77 ± 0.34	17.65	-2.36 ± 1.31	-5.00
LLFN	-71.788	-39.333	-11.20 ± 0.41	-12.53	7.86 ± 0.35	7.69	-1.74 ± 1.13	-3.66
LNDS	-70.575	-32.839	-14.27 ± 0.42	-15.38	-9.50 ± 0.17	-9.34	-1.53 ± 1.00	-4.83
MOCH	-73.904	-38.410	-120.39 ± 0.77	-120.36	-29.45 ± 0.40	-29.45	20.29 ± 1.28	20.27
NIEB	-73.401	-39.868	-0.49 ± 0.55	-1.76	-2.90 ± 0.46	-3.67	-1.26 ± 1.25	-4.43

Table S2: InSAR data used in this study.

track ID	orbit ID reference/repeat	acquisition dates reference/repeat[a]	perpendicular baseline[b] (m)	frames	observation mode	comments
ascending tracks						
T111	07119/21881	5/27/07--3/4/2010	215	6480--6520	FBS-FBS	
T112	21458/22129	2/3/10--3/21/2010	485	6470--6500	FBS-FBS	propagation phase delay
T113	10970/21706	2/15/08--4/7/2010	274	6470-6500	FBS-FBS	more recent pair is noisy
T114	21283/21954	1/22/10--3/9/10	284	6460--6480	FBS-FBS	
T115	21531/22202	2/8/10--5/11/2010	409	6470	FBS-FBS	PRF change[c]
T116	21779/22450	2/25/2010--4/12/10	480	6460	FBS-FBS	propagation phase delay
T117	09949/22027	12/7/07--3/14/10	157	6420-6440	FBS-FBS	low coherence
T118	21604/22275	2/13/2010--3/31/10	717	6410--6430	FBS-FBS	
T119	21181/21852	1/15/10--3/2/10	453	6400--6420	FBS-FBS	
descending tracks						
T422-sw3	11779/21844	4/10/08--3/1/10	1411	4350	ScanSAR-ScanSAR[d]	low coherence
T422-sw4	21173/21844	1/14/10--3/1/2010	560	4300-4400	FBS-ScanSAR[e]	
T420	21348/22019	1/26/10--3/13/2010	517	4330-4400	FBS-FBS	

[a] short time span (i.e., one orbit cycle) between reference and repeat passes is preferred to measure coseismic deformation
[b] short perpendicular baseline is preferred to remove topography phase noise
[c] PRF means Pulse Repetition Frequency
[d] See text for details
[e] See text for details

Table S3. Shear modulus structure in Maule, Chile region [after *Bohm et al*., 2002].

depth (km)	V_p (km/s)	V_s (km/s)	density (kg/m^3)	shear modulus (GPa)
-2 - 0	4.39	2.4	2100	12.1
0 - 5	5.51	3.19	2600	21.4
5 - 20	6.28	3.6	2800	36.3
20 - 35	6.89	3.93	2800	43.2
35 - 45	7.4	4.12	2800	47.5
45 - 55	7.76	4.55	3300	68.3
55 - 90	7.94	4.55	3300	68.3
90 - ∞	8.34	4.77	3300	75.1